

BATTERIES

Atomic structure of sensitive battery materials and interfaces revealed by cryo-electron microscopy

Yuzhang Li,^{1*} Yanbin Li,^{1*} Allen Pei,¹ Kai Yan,¹ Yongming Sun,¹ Chun-Lan Wu,¹ Lydia-Marie Joubert,² Richard Chin,³ Ai Leen Koh,³ Yi Yu,⁴ John Perrino,² Benjamin Butz,^{1,5} Steven Chu,^{6,7} Yi Cui^{1,8†}

Whereas standard transmission electron microscopy studies are unable to preserve the native state of chemically reactive and beam-sensitive battery materials after operation, such materials remain pristine at cryogenic conditions. It is then possible to atomically resolve individual lithium metal atoms and their interface with the solid electrolyte interphase (SEI). We observe that dendrites in carbonate-based electrolytes grow along the $\langle 111 \rangle$ (preferred), $\langle 110 \rangle$, or $\langle 211 \rangle$ directions as faceted, single-crystalline nanowires. These growth directions can change at kinks with no observable crystallographic defect. Furthermore, we reveal distinct SEI nanostructures formed in different electrolytes.

A typical lithium-ion battery consists of a negative electrode (anode), a positive electrode (cathode), a polymer separator, and an organic liquid electrolyte. Although each battery component is macroscopic in practice, research has focused on the microscopic, nanoscopic, and atomistic features to probe more fundamental aspects of battery operation. Transmission electron microscopy (TEM) has been used to study battery materials (1–8), but imaging was limited to samples with reasonable stability under an electron beam. Many battery components [e.g., some lithium-containing electrode

materials, organic liquid electrolytes, solid electrolyte interphase (SEI) layer] are chemically reactive and sensitive to electron-beam irradiation, so TEM studies of batteries in their native environment are problematic.

In particular, both Li metal and the organic liquid electrolyte are unstable during battery charge and discharge. Li metal is repeatedly deposited and stripped during battery operation, resulting in large structure changes that are exacerbated by dendrite growth (9). The organic electrolyte decomposes onto the surfaces of battery anodes (10–12) (e.g., Li metal, silicon, graph-

ite, etc.) by an electrochemically driven process to form a SEI layer composed of organic (e.g., polymeric) and inorganic (e.g., carbonates, oxides, fluorides) components. These two phenomena are intimately related. The fragile SEI influences the structure of the Li metal, which, if unstable, will result in SEI fracture and continued electrolyte consumption. Elucidating the Li metal and SEI nanostructure is critical for developing potential solutions to these failure modes.

Unfortunately, current understanding is limited to ensemble studies using low-resolution TEM (6–8), indirect-imaging (13, 14), and surface-sensitive (15, 16) techniques. Although the general morphology of Li dendrites and chemical composition of the SEI can be observed, their detailed nanostructure and crystallography are important aspects that have not been explored on the single-particle level. For example, the distribution of organic and inorganic components in the SEI layer and their effect on dendrite growth cannot be explained without spatially

¹Department of Materials Science and Engineering, Stanford University, Stanford, CA 94305, USA. ²Cell Sciences Imaging Facility, Stanford University School of Medicine, Stanford, CA 94305, USA. ³Stanford Nano Shared Facility, Stanford University, Stanford, CA 94305, USA. ⁴School of Physical Science and Technology, ShanghaiTech University, Shanghai 201210, China. ⁵Institut für Werkstofftechnik and Gerätezentrum für Mikro- und Nanoanalytik (MNaF), Universität Siegen, 57068 Siegen, Germany. ⁶Department of Physics, Stanford University, Stanford, CA 94305, USA. ⁷Department of Molecular and Cellular Physiology, Stanford University School of Medicine, Stanford, CA 94305, USA. ⁸Stanford Institute for Materials and Energy Sciences, Stanford Linear Accelerator Center (SLAC) National Accelerator Laboratory, Menlo Park, CA 94025, USA. *These authors contributed equally to this work.

†Corresponding author. Email: yicui@stanford.edu

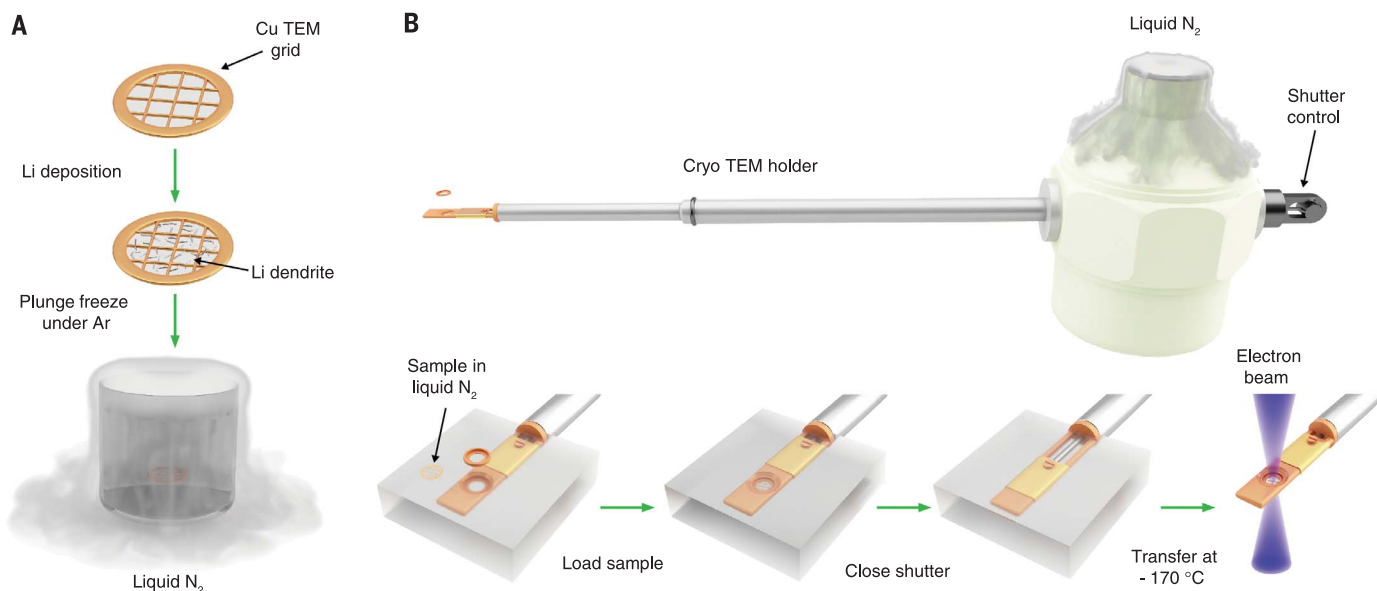


Fig. 1. Preserving and stabilizing Li metal by cryo-EM. (A) Li metal dendrites are electrochemically deposited directly onto a Cu TEM grid and then plunged into liquid nitrogen after battery disassembly. (B) The specimen is then placed onto the cryo-TEM holder while still immersed in

liquid nitrogen and isolated from the environment by a closed shutter. During insertion into the TEM column, temperatures do not increase above -170°C , and the shutter prevents air exposure to the Li metal.

resolving these structures at the nanoscale. However, because of sample damage from high electron dose rates necessary for high-resolution imaging (figs. S6 and S7), single-particle studies of pristine Li metal and the SEI have not been possible. Here we use cryo-electron microscopy (EM) techniques to characterize the detailed structure of Li metal and its SEI, demonstrating

that atomic-resolution imaging of sensitive battery materials in their native state is possible at cryogenic conditions.

At room temperature, Li metal is very reactive and corrodes upon brief air exposure (17) during sample transfer into the TEM column. Additionally, a low melting point and weak atomic bonding make the light Li atoms extremely unstable

under an electron beam (18). To overcome these challenges, we developed a cryo-transfer method (Fig. 1) based on cryo-EM procedures used in structural biology. First, we electrochemically deposit Li metal onto a copper TEM grid using standard battery conditions (figs. S1 and S13). We then wash the grid with electrolyte and immediately flash-freeze the specimen in liquid

Fig. 2. Atomic-resolution TEM of Li metal dendrites.

(A) Cryo-EM image of Li metal dendrites. Electron dose rate $<1 \text{ e} \text{ \AA}^{-2} \text{ s}^{-1}$. **(B)** Standard TEM image of Li metal dendrite with $\sim 1 \text{ s}$ air exposure at room temperature. Inset, corresponding SAED pattern. **(C)** Standard TEM image of the dendrite from (B) after exposure to electron dose rate of $\sim 500 \text{ e} \text{ \AA}^{-2} \text{ s}^{-1}$ for $\sim 1 \text{ s}$. The three holes were formed immediately after this exposure. **(D)** Time-lapse images of Li dendrite from the green-outlined area in (A) after continuous electron-beam irradiation at a dose rate of $\sim 50 \text{ e} \text{ \AA}^{-2} \text{ s}^{-1}$. **(E and H)** TEM images of Li metal dendrites growing along the $\langle 211 \rangle$ (E) and $\langle 110 \rangle$ (H) directions. Inset, corresponding SAED pattern showing that the dendrites are single-crystalline. Electron dose rate $<1 \text{ e} \text{ \AA}^{-2} \text{ s}^{-1}$ for $\sim 30 \text{ s}$. **(F and I)** Magnified image of boxed regions in red (F) and blue (I) from (E) and (H), respectively, showing the Li metal lattice at high resolution. Electron dose rate $\sim 1000 \text{ e} \text{ \AA}^{-2} \text{ s}^{-1}$ for $\sim 30 \text{ s}$. **(G and J)** Atomic-resolution TEM images resolving individual Li atoms along the $[111]$ (G) and $[001]$ (J) zone axes. Electron dose rate $\sim 1000 \text{ e} \text{ \AA}^{-2} \text{ s}^{-1}$ for $\sim 30 \text{ s}$.

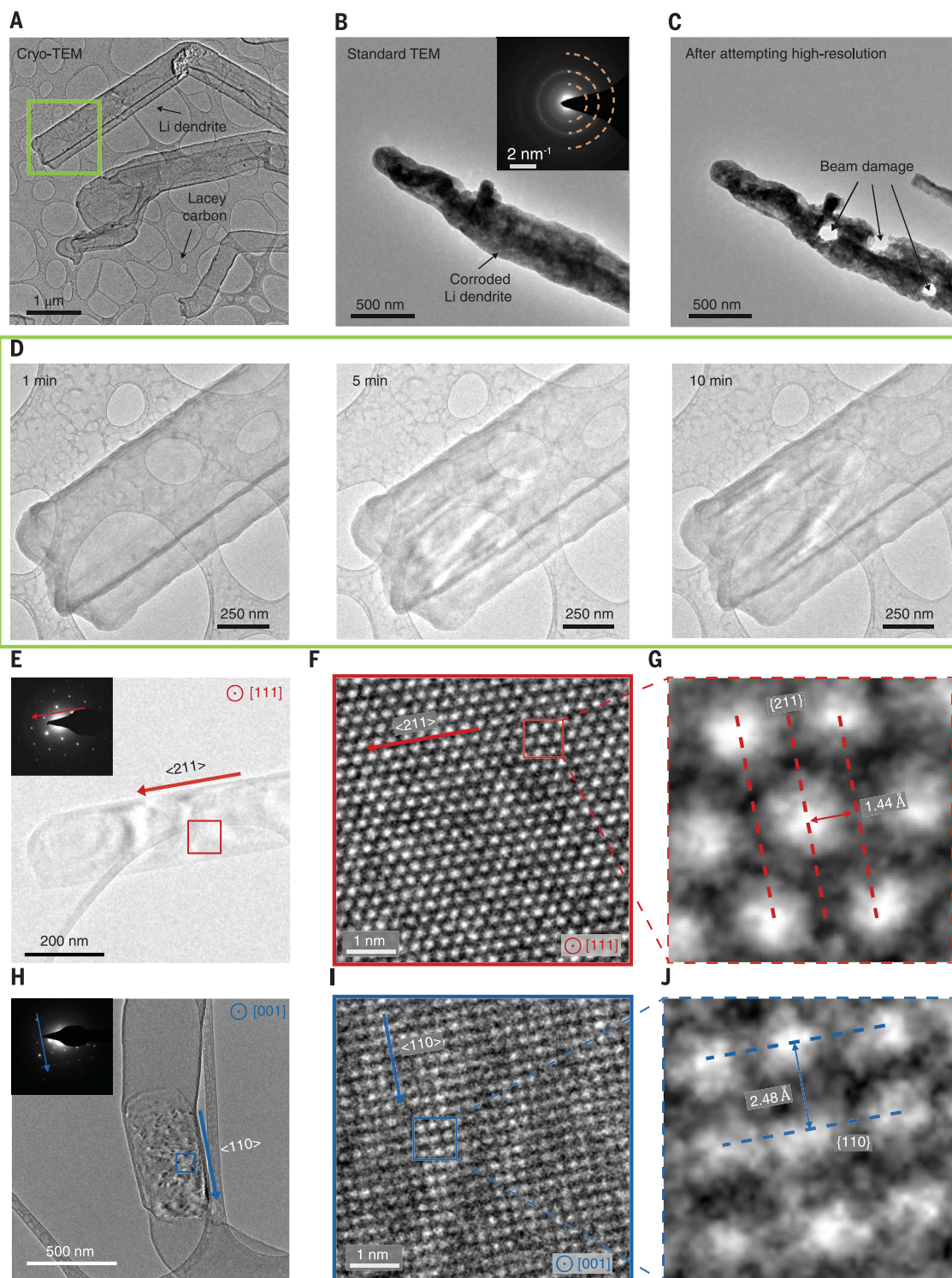
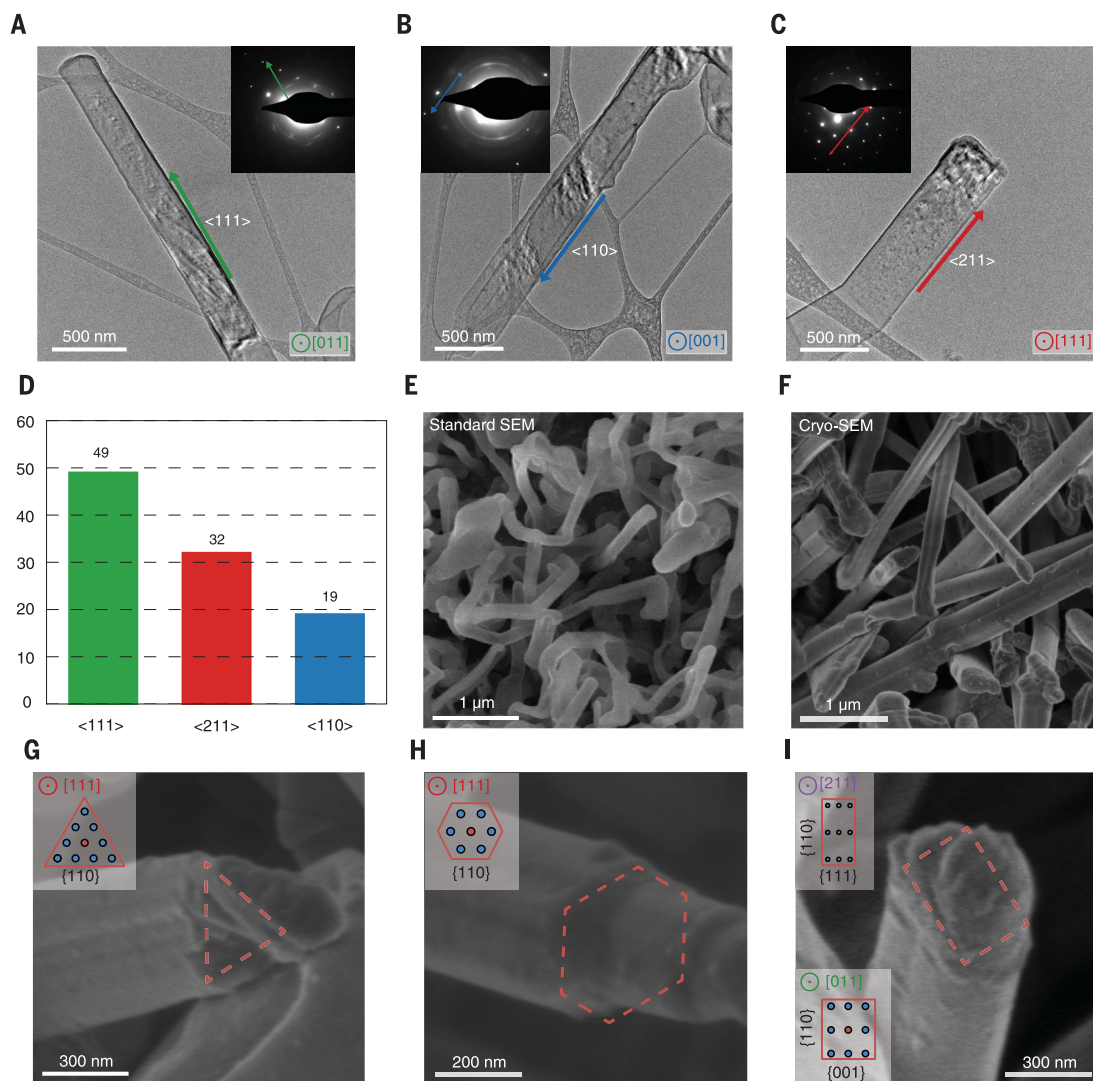


Fig. 3. Faceting behavior of Li metal dendrites.

(A to C) Li metal dendrites and their corresponding SAED patterns (insets) growing along $\langle 111 \rangle$ (A), $\langle 110 \rangle$ (B), and $\langle 211 \rangle$ (C). Electron dose rate $< 1 e \text{ \AA}^{-2} \text{ s}^{-1}$ for ~ 30 s. (D) Statistics showing preferred growth direction is along $\langle 111 \rangle$. (E) Standard SEM image of Li metal dendrites after brief exposure to air.

Facets cannot be observed because of corrosion in air. (F) Cryo-SEM image of Li metal dendrites. Facet morphology is preserved by the cryo-transfer method. (G to I) Diagram of triangular (G), hexagonal (H), and rectangular (I) cross-sectional structures for dendrites, exhibiting clear faceting behavior. The low-energy (110) facet should be exposed according to thermodynamic considerations. Insets, diagrams of atomic projections from various zone axes. The shapes correspond to the cross-sectional structures observed in cryo-SEM.



nitrogen (19). At cryogenic temperatures, Li metal does not react with the liquid nitrogen or ice so that the dendrites retain their electrochemical state with the relevant structural and chemical information preserved. Because we directly visualize individual dendrite structures instead of reconstructing three-dimensional models (necessary for biomolecules), atomic resolutions of 0.7 \AA are possible (20, 21) for the spherical aberration-corrected TEM (operating at 300 kV) used in our experiments.

Figure 2A is a cryo-EM image of Li metal dendrites formed after the first electrochemical deposition. In general, sample regions were exposed to electron (e) dose rates of $\sim 1000 e \text{ \AA}^{-2} \text{ s}^{-1}$ for ~ 30 s in high-resolution images and $< 1 e \text{ \AA}^{-2} \text{ s}^{-1}$ for ~ 30 s in low-resolution images (details in figure captions). In Fig. 2A, the dendritic structures appear much lighter in contrast than the lacey carbon (atomic number 6) from the TEM grid, suggesting that they have a lower atomic number. Electron energy-loss spectroscopy and energy-filtered TEM data confirm the identity of these

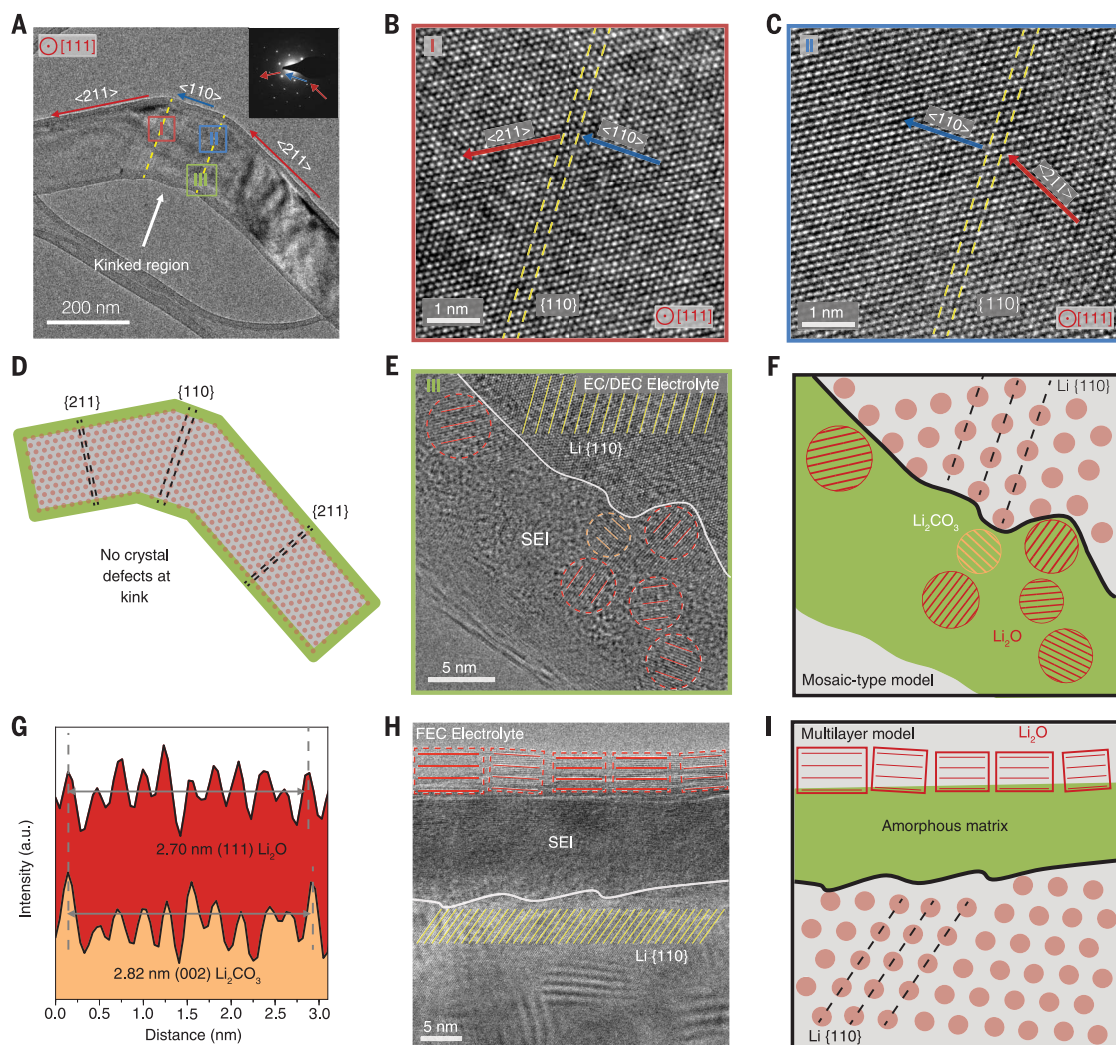
dendritic structures as Li metal (figs. S12 and S16), indicating that the dendrites were successfully preserved during the cryo-transfer. A smooth and thin layer (thickness ~ 10 nm) appearing slightly darker in contrast is identified as the SEI layer that forms on Li metal during battery cycling. In contrast to cryo-transferred samples, Li metal that was inserted into the TEM at room temperature (19) was quickly consumed by environmental exposure (Fig. 2B). These air-exposed Li dendrites have a much rougher surface and darker contrast than the cryo-transferred Li dendrites because of the formation of polycrystalline artifacts, as shown by the corresponding selected-area electron diffraction (SAED; Fig. 2B, inset). The main rings in the SAED pattern of Fig. 2B (outlined in orange) correspond to lattice spacings of 4.38, 2.76, and 2.56 \AA , indicating the presence of lithium hydroxide (22). Furthermore, any attempt to image Li metal dendrites using standard TEM at high resolution (electron dose rate $\sim 500 e \text{ \AA}^{-2} \text{ s}^{-1}$ for ~ 1 s) results in sample destruction, as evidenced by the holes burned into the Li dendrite from the

electron beam (Fig. 2C). These control experiments illustrate major reasons why atomically resolved images of Li metal have not been possible under standard TEM conditions.

Figure 2D shows time-lapse images of the dendrite from Fig. 2A (boxed in green) under constant electron-beam irradiation at dose rates of $\sim 50 e \text{ \AA}^{-2} \text{ s}^{-1}$ in cryogenic conditions. No damage in dendrite morphology is detected even after 10 min. Two such dendrites and their corresponding SAED patterns are shown in Fig. 2, E and H. With the TEM tuned for rotational calibration (figs. S8 and S9), we can index their SAED patterns to the body-centered cubic (BCC) crystal structure of Li metal with the zone axis along the $[111]$ (Fig. 2E) and $[100]$ directions (Fig. 2H). This analysis allows us to assign the growth direction (long axis) of these dendrites to be along $\langle 211 \rangle$ and $\langle 110 \rangle$ for Fig. 2, E and H, respectively.

High-resolution images of the Li metal dendrites (Fig. 2, F and I) at cryogenic temperatures resolve individual Li atoms, showing that the Li dendrites are single crystalline. All high-resolution

Fig. 4. Atomic-resolution TEM of kinked Li metal dendrite and SEI interface. (A) TEM image of kinked Li metal dendrite that changes from a $\langle 211 \rangle$ to $\langle 110 \rangle$ and back to $\langle 211 \rangle$ growth direction. Inset shows corresponding SAED pattern. Electron dose rate $<1 \text{ e} \text{ \AA}^{-2} \text{ s}^{-1}$ for $\sim 30 \text{ s}$. The dashed yellow lines indicate change in growth direction. (B and C) Magnified images of red region I (B) and blue region II (C) outlined in (A) showing both kinks at high resolution. Electron dose rate $\sim 1000 \text{ e} \text{ \AA}^{-2} \text{ s}^{-1}$ for $\sim 30 \text{ s}$. (D) Schematic of the single-crystalline nature of the kink. (E) Atomic-resolution image of green region III outlined in (A) revealing the interface between Li metal and the SEI. The lattice spacings of small crystalline grains of inorganic material dispersed throughout the amorphous film can be matched to Li carbonate (Li_2CO_3 , orange circles) and Li oxide (Li_2O , red circles). Electron dose rate $\sim 1000 \text{ e} \text{ \AA}^{-2} \text{ s}^{-1}$ for $\sim 30 \text{ s}$. (F) Schematic of the observed mosaic-type structure formed on Li dendrites in EC-DEC electrolyte. (G) Integrated pixel intensities of Li oxide (red) and Li carbonate (orange) lattice. The peaks and valleys represent rows of atoms and the gaps, respectively. a.u., arbitrary units. (H) Atomic-resolution image of the SEI



formed in FEC electrolyte. Electron dose rate $\sim 1000 \text{ e} \text{ \AA}^{-2} \text{ s}^{-1}$ for $\sim 30 \text{ s}$. (I) Schematic of the observed multilayered structure formed on Li dendrites in FEC electrolyte.

TEM images were taken under negative C_s (spherical aberration) imaging conditions with a defocus value of ~ 5 to 8 nm and a C_s value of $\sim 15 \mu\text{m}$. Image simulations confirm that the areas of bright contrast correspond to atomic columns (figs. S10 and S11) (19). At the atomic scale, the dendrite growth directions are visible and parallel the directions previously assigned at lower magnifications. From the atomic-resolution images (Fig. 2, G and J), we measure the lattice spacings of the $\{110\}$ and $\{211\}$ planes to be 2.48 and 1.44 \AA , respectively (fig. S2). These measurements match well with previous x-ray diffraction data on bulk Li metal, with values of 2.48 and 1.43 \AA for the $\{110\}$ and $\{211\}$ planes, respectively (23). Despite prolonged imaging ($\sim 30 \text{ s}$) at electron dose rates of $\sim 1000 \text{ e} \text{ \AA}^{-2} \text{ s}^{-1}$, the Li atoms from the acquired images remain stable.

Our observation that Li metal dendrites grow as single-crystalline nanowires along different directions is a surprising one. Therefore, we con-

ducted structural characterization of many dendrites (~ 100) to further investigate their growth behavior. We observed three primary growth directions along $\langle 111 \rangle$, $\langle 110 \rangle$, and $\langle 211 \rangle$, whose representative TEM images with their corresponding SAED patterns are shown in Fig. 3, A, B, and C, respectively. The data show a preference (49% by number) for Li metal dendrites to grow along the $\langle 111 \rangle$ direction in carbonate-based electrolyte (Fig. 3D), followed by $\langle 211 \rangle$ (32%) and $\langle 110 \rangle$ (19%). The apparent growth preference along $\langle 111 \rangle$ can be rationalized by considering Li surface energies. In the BCC crystal structure, the $\{110\}$ family of planes is the most densely packed and thus has the lowest-energy surface according to the broken bond model (24). Thermodynamically, we expect a single-crystalline Li metal dendrite to favor facets exposing the $\{110\}$ planes as the side surface. For detailed observations of the dendrite facets, scanning electron microscopy (SEM) is complementary to TEM owing to its

large depth of field. Faceting behavior is difficult to observe using standard techniques because side reactions in ambient air corrode the sharp-angled facets, forming curved surfaces shown in typical ex situ SEM images (Fig. 3E). We adopted our cryo-transfer method to SEM (19) and observed the growth facets on Li metal, confirming the dendrite morphology (Fig. 3F), with triangular (Fig. 3G), hexagonal (Fig. 3H), and rectangular (Fig. 3I) cross-sectional Li dendrite structures. In the BCC crystal system, a triangular or hexagonal cross section is appropriate for dendrites growing along $\langle 111 \rangle$, as all three or six of the facets would expose $\{110\}$ planes and thus minimize the dendrite surface energy (Fig. 3, G and H, insets). When tilted to a grazing angle, a dendrite growing along $\langle 111 \rangle$ in the TEM appears to have a hexagonal cross section (fig. S3). For dendrites growing along $\langle 211 \rangle$ or $\langle 110 \rangle$, the sidewalls cannot all expose $\{110\}$ facets (Fig. 3I, insets). However, by maximizing the surface area

of their existing {110} facets, <211> and <110> dendrites can reduce their surface energy, elongating the rectangular cross section into the observed ribbonlike structure. Our data here suggest that surface energies of the facets play a large role in influencing the Li dendrite growth direction. However, the system is complicated by the existence of an SEI layer, conditions of battery cycling, and the electrolyte used, parameters that all may affect the surface energy and, thus, growth direction.

In the carbonate-based electrolyte system, Li metal dendrites do not always grow as straight single-crystalline nanowires along a linear direction. They will often change crystallographic growth directions at regions we refer to as kinks. In Fig. 4A, one such kinked region is shown to change between the <211> and <110> growth directions. Starting from the right, the Li metal dendrite initially grows along <211> and changes to <110> at the first kink (dashed yellow line). After growing along <110>, the growth direction switches to a different orientation of <211> at the second kink. Atomic-resolution TEM images of the left and right kink are shown in Fig. 4, B and C, respectively. There are no observable crystal defects at either kinked region. This contrasts with other nanowire crystal systems, in which defects like twin boundaries or stacking faults typically govern changes in growth directions (25–30). For the BCC crystal structure of Li metal, however, defects are not a prerequisite for switching between the <211> and <110> growth directions. The schematic in Fig. 4D depicts the atomic structure of the kinked dendrite (not to scale) as reconstructed from the atomic-resolution images (Fig. 4, B and C). From this diagram, a defect-free transition from <211> to <110> and back to <211> is possible if the kinks have an angle of 30°, the theoretical angle between the <110> and <211> direction in a pristine BCC lattice; this is observed for both kinks from Fig. 4A. Thus, the Li metal dendrite remains single crystalline despite kinking, as further evidenced by the SAED pattern (Fig. 4A, inset). The reason for kinking may be due to a variation of the SEI composition and/or structure during the growth of Li dendrites.

To determine the structure and composition of various SEI films, we investigated the SEI formed in (i) a standard electrolyte and (ii) an electrolyte mixed with a fluorine-functionalized additive. The SEI layer formed in the widely used carbonate-based electrolyte ethylene carbonate–diethyl carbonate (EC–DEC) is shown in Fig. 4E and fig. S14. From the atomic interface between Li metal and the SEI, it is observed that the SEI contains small crystalline domains (diameter ~3 nm) dispersed randomly throughout an amorphous matrix that coats the Li metal. These crystalline grains are the inorganic components of the SEI, identified to be Li oxide and Li carbonate by matching their lattice spacings (Fig. 4G). The amorphous matrix is likely the organic polymer formed by carbonate electrolyte decomposition. The SEI formed in this standard electrolyte resembles the mosaic structure predicted by Peled

et al. (31), which describes the SEI as a heterogeneous distribution of inorganic and organic components (Fig. 4F). We observe a completely different SEI structure (Fig. 4H and fig. S15) when it is formed in a carbonate-based electrolyte with 10 volume % fluoroethylene carbonate (FEC), a common additive used for improving battery performance (32). Instead of a random distribution of organic and inorganic components, the SEI formed in the presence of FEC is more ordered and appears to have a multilayer structure, consistent with the multilayer system proposed by Aurbach *et al.* (33). The inner layer appears to be an amorphous polymer matrix, whereas the outer layer is determined to be large grains (~15 nm) of Li oxide with clear lattice fringes. The Li fluoride (LiF) lattice cannot be detected, even though LiF is considered to be a primary reason for performance enhancement (34).

We further probed the chemical composition of both SEI structures using energy-dispersive x-ray (EDX) spectroscopy. Dendrites remain undamaged after 5 min of continuous EDX spectra collection with electron dose rates of ~100 e Å⁻² s⁻¹ (fig. S4). No obvious difference in chemical composition can be detected for either the SEI formed in fluoroethylene (FEC) additive or standard EC–DEC electrolyte (fig. S5). Both EDX spectra have similar intensities for fluorine, which likely forms by decomposition of the Li hexafluorophosphate salt used in both electrolytes (12). The only clear difference between these SEI layers is the distribution and arrangement of their chemical species. Thus, the favorable effect of the FEC additive may be due to its influence on forming a more-ordered SEI nanostructure. We hypothesize that the ordered nature of a multilayer structure can offer increased mechanical durability, making it more robust during battery cycling, whereas a random distribution of inorganics is more likely to fracture during cycling.

This work presents a simple methodology to preserve and image sensitive battery materials with atomic resolution, revealing detailed nanostructures. The insight gained from these experiments can lead to a more complete understanding of the failure mechanisms in high-energy batteries. For example, changes in SEI nanostructure and dendrite crystallography formed in different environments can potentially explain the efficacy of certain electrolyte systems. Although we use Li metal as an example to demonstrate the utility of cryo-EM, the experiments described here can potentially be extended for other studies involving beam-sensitive materials, such as lithiated silicon or sulfur.

REFERENCES AND NOTES

1. J. Y. Huang *et al.*, *Science* **330**, 1515–1520 (2010).
2. X. H. Liu *et al.*, *Nat. Nanotechnol.* **7**, 749–756 (2012).
3. F. Wang *et al.*, *Nat. Commun.* **3**, 1201 (2012).
4. M. Gu *et al.*, *Nano Lett.* **13**, 6106–6112 (2013).
5. Z. Zeng *et al.*, *Nano Lett.* **14**, 1745–1750 (2014).
6. B. L. Mehdi *et al.*, *Nano Lett.* **15**, 2168–2173 (2015).

7. R. L. Sacci *et al.*, *Nano Lett.* **15**, 2011–2018 (2015).
8. A. J. Leenheer, K. L. Jungjohann, K. R. Zavadil, J. P. Sullivan, C. T. Harris, *ACS Nano* **9**, 4379–4389 (2015).
9. C. Brissot, M. Rosso, J.-N. Chazalviel, S. Lascaud, *J. Power Sources* **81–82**, 925–929 (1999).
10. E. Peled, *J. Electrochem. Soc.* **126**, 2047–2051 (1979).
11. D. Aurbach, M. L. Daroux, P. W. Faguy, E. Yeager, *J. Electrochem. Soc.* **134**, 1611–1620 (1987).
12. K. Xu, *Chem. Rev.* **104**, 4303–4418 (2004).
13. R. Bhattacharyya *et al.*, *Nat. Mater.* **9**, 504–510 (2010).
14. K. J. Harry, D. T. Hallinan, D. Y. Parkinson, A. A. MacDowell, N. P. Balsara, *Nat. Mater.* **13**, 69–73 (2014).
15. D. Aurbach, *J. Power Sources* **89**, 206–218 (2000).
16. S. J. An *et al.*, *Carbon* **105**, 52–76 (2016).
17. M. M. Markowitz, D. A. Boryta, *J. Chem. Eng. Data* **7**, 586–591 (1962).
18. R. F. Egerton, P. Li, M. Malac, *Micron* **35**, 399–409 (2004).
19. Materials and methods are available as supplementary materials.
20. M. Haider *et al.*, *Ultramicroscopy* **75**, 53–60 (1998).
21. K. W. Urban, *Science* **321**, 506–510 (2008).
22. H. E. Swanson, E. Tatge, *Standard X-ray Diffraction Powder Patterns: Vol. 1, Data for 54 Inorganic Substances* (U.S. Department of Commerce, National Bureau of Standards, Washington, DC, June 1953).
23. M. R. Nadler, C. P. Kempier, *Anal. Chem.* **31**, 2109–2109 (1959).
24. L. Vitos, A. V. Ruban, H. L. Skriver, J. Kollar, *Surf. Sci.* **411**, 186–202 (1998).
25. M. H. Huang *et al.*, *Adv. Mater.* **13**, 113–116 (2001).
26. P. X. Gao *et al.*, *Science* **309**, 1700–1704 (2005).
27. J. Johansson *et al.*, *Nat. Mater.* **5**, 574–580 (2006).
28. R. E. Algra *et al.*, *Nature* **456**, 369–372 (2008).
29. P. Caroff *et al.*, *Nat. Nanotechnol.* **4**, 50–55 (2009).
30. B. Tian, P. Xie, T. J. Kempa, D. C. Bell, C. M. Lieber, *Nat. Nanotechnol.* **4**, 824–829 (2009).
31. E. Peled, D. Golodnitsky, G. Ardel, *J. Electrochem. Soc.* **144**, L208–L210 (1997).
32. F. Ding *et al.*, *J. Electrochem. Soc.* **160**, A1894–A1901 (2013).
33. D. Aurbach, Y. Ein-Ely, A. Zaban, *J. Electrochem. Soc.* **141**, L1–L3 (1994).
34. Q. C. Liu *et al.*, *Adv. Mater.* **27**, 5241–5247 (2015).

ACKNOWLEDGMENTS

The authors thank D. Bushnell and D.-H. Chen for facilitating cryo-EM capabilities and A. F. Marshall for fruitful discussions. Yu.L. acknowledges the National Science Foundation Graduate Research Fellowship Program for funding. A.P. acknowledges support from the National Defense Science and Engineering Graduate Fellowship and the Stanford Graduate Fellowship. B.B. acknowledges financial support by the German Research Foundation (DFG) under grant no. BU 2875/2-1. Y.C. acknowledges support from the Assistant Secretary for Energy Efficiency and Renewable Energy, Office of Vehicle Technologies of the U.S. Department of Energy, under the Battery Materials Research Program and Battery 500 Consortium Programs. Yu.L., Ya.L., and Y.C. conceived the idea and designed the experiments. A.L.K. and J.P. helped set up cryo-EM instrumentation. Yu.L. and Ya.L. conducted electrochemical and cryo-EM characterization. L.-M.J. and R.C. helped with cryo-SEM characterization. Y.S. and C.-L.W. worked on other characterizations. Y.Y. completed image simulations. B.B. assisted with spectroscopic and chemical mapping experiments. Yu.L., Ya.L., A.P., K.Y., and Y.C. interpreted the results. Yu.L., Ya.L., S.C., and Y.C. co-wrote the paper. All authors discussed the results and commented on the manuscript.

SUPPLEMENTARY MATERIALS

www.sciencemag.org/content/358/6362/506/suppl/DC1
Materials and Methods
Supplementary Text
Figs. S1 to S16
References (35–40)

15 December 2016; accepted 14 September 2017
10.1126/science.aam6014

Atomic structure of sensitive battery materials and interfaces revealed by cryo-electron microscopy

Yuzhang Li, Yanbin Li, Allen Pei, Kai Yan, Yongming Sun, Chun-Lan Wu, Lydia-Marie Joubert, Richard Chin, Ai Leen Koh, Yi Yu, John Perrino, Benjamin Butz, Steven Chu and Yi Cui

Science **358** (6362), 506-510.
DOI: 10.1126/science.aam6014

Frozen in time

The electrochemical processes occurring in a battery are highly dynamic. To understand the complexities of the charge and discharge cycles, you need to be able to watch the processes in situ or to freeze the battery rapidly for ex situ analysis. Li *et al.* applied cryo-electron microscopy techniques commonly used for studying biological samples to examine batteries. They identified the solid electrolyte interphase that forms, observed the interactions of Li with the interphase, and captured the formation of dendrites that can be detrimental to the lifetime of a battery.

Science, this issue p. 506

ARTICLE TOOLS

<http://science.sciencemag.org/content/358/6362/506>

SUPPLEMENTARY MATERIALS

<http://science.sciencemag.org/content/suppl/2017/10/26/358.6362.506.DC1>

REFERENCES

This article cites 37 articles, 10 of which you can access for free
<http://science.sciencemag.org/content/358/6362/506#BIBL>

PERMISSIONS

<http://www.sciencemag.org/help/reprints-and-permissions>

Use of this article is subject to the [Terms of Service](#)